



# Numerical and theoretical investigations of heat transfer characteristics in helium–xenon cooled microreactor core

Tian-Shi Wang<sup>1</sup> · Xiang Chai<sup>1</sup> · Chao-Ran Guan<sup>1</sup> · Xin-Yue Liu<sup>1</sup> · Jiao-Long Deng<sup>1</sup> · Hui He<sup>1</sup> · Xiao-Jing Liu<sup>1</sup>

Received: 5 May 2023 / Revised: 6 July 2023 / Accepted: 7 July 2023 / Published online: 14 November 2023

© The Author(s), under exclusive licence to China Science Publishing & Media Ltd. (Science Press), Shanghai Institute of Applied Physics, the Chinese Academy of Sciences, Chinese Nuclear Society 2023

## Abstract

Helium–xenon cooled microreactors are a vital technological solution for portable nuclear reactor power sources. To examine the convective heat transfer behavior of helium–xenon gas mixtures in a core environment, numerical simulations are conducted on a cylindrical coolant channel and its surrounding solid regions. Validated numerical methods are used to determine the effect and mechanisms of power and its distribution, inlet temperature and velocity, and outlet pressure on the distribution and change trend of the axial Nusselt number. Furthermore, a theoretical framework that can describe the effect of power variation on the evolution of the thermal boundary layer is employed to formulate an axial distribution correlation for the Nusselt number of the coolant channel, under the assumption of a cosine distribution for the axial power. Based on the simulation results, the correlation coefficients are determined, and a semi-empirical relationship is identified under the corresponding operating conditions. The correlation derived in this study is consistent with the simulations, with an average relative error of 5.3% under the operating conditions. Finally, to improve the accuracy of the predictions near the entrance, a segmented correlation is developed by combining the Kays correlation with the aforementioned correlation. The new correlation reduces the average relative error to 2.9% and maintains satisfactory accuracy throughout the entire axial range of the channel, thereby demonstrating its applicability to turbulent heat transfer calculations for helium–xenon gas mixtures within the core environment. These findings provide valuable insights into the convective heat transfer behavior of a helium–xenon gas mixture in a core environment.

**Keywords** Helium–xenon gas mixture · Convective heat transfer · Power distribution · Numerical simulation · Nusselt number correlation

## Abbreviations

$A$	Cross-sectional area of coolant channel ( $\text{m}^2$ )
$a_n$	Coefficients in Eq. 13
$C$	Constant in Eq. 1
$C_p$	Specific heat at constant pressure ( $\text{J}/(\text{kg}\cdot\text{K})$ )
$e$	Constant in Pickett's correlation
$F_n$	Coefficients in series expansion of wall temperature

$f$	Friction factor
$G$	Radial variation of fully developed temperature profile
$h$	Convective heat transfer coefficient ( $\text{W}/(\text{m}^2\cdot\text{K})$ )
$k$	Thermal conductivity ( $\text{W}/(\text{m}\cdot\text{K})$ )
$L$	Hydraulic diameter of coolant channel (m)
$m$	Mass flow rate (kg/s)
$Nu$	Nusselt number
$\Delta Nu$	10% Of average $Nu$ obtained in each run
$P$	Pressure of standard condition (MPa)
$Pr$	Prandtl number
$Pe$	Peclet number
$Q$	Power of standard condition (W)
$q$	Heat flux ( $\text{W}/\text{m}^2$ )
$Re$	Reynolds number
$r_0^+$	Dimensionless coolant channel radius
$T$	Inlet temperature of standard condition (K)
$t$	Temperature (K)
$U$	Velocity of standard condition (m/s)

The work was supported by the National Key R&D Program of China (No. 2020YFB1901900), the National Natural Science Foundation of China (No. 12275175), the Special Fund for Strengthening Industry of Shanghai (No. GYQJ-2018-2-02), the Shanghai Rising Star Program (No. 21QA1404200), and the Ling Chuang Research Project of the China National Nuclear Corporation.

✉ Xiang Chai  
xiangchai@sjtu.edu.cn

<sup>1</sup> School of Nuclear Science and Engineering, Shanghai Jiao Tong University, Shanghai 200240, China

$u$	Velocity (m/s)
$z$	Axial distance from inlet (m)
$\tilde{z}$	Axial distance between end point of integral and inlet (m)

#### Greek letters

$\alpha$	Constant in Eq. 10
$\beta_n$	Eigenvalues
$\gamma$	Distance required downstream of first measuring point to observe a decrease in $\Delta Nu$
$\delta$	Distance required upstream of last measuring point to observe an increase in $\Delta Nu$
$\varepsilon$	Eddy diffusivity ( $\text{m}^2/\text{s}$ )
$\mu$	Viscosity (Pa·s)
$\pi$	Circular constant
$\rho$	Density ( $\text{kg}/\text{m}^3$ )
$\varphi$	Simplified $F_n$
$\omega$	Simplified $a_n$

#### Subscripts

avg	Average
b	Bulk
cor	Calculated by correlation
in	Inlet
m	Momentum
out	Outlet
sim	Calculated via simulation
t	Turbulent
w	Wall

## 1 Introduction

Nuclear microreactors typically generate up to 20 MW<sub>th</sub> of power and offer numerous advantages, including flexible siting, long operational endurance, high safety level, and high reliability [1]. They can provide power and heat to both industrial facilities and remote communities, and are promising for use in deep-space and deep-sea exploration [2]. To develop microreactors that can generate megawatt-level electrical power, scientists typically employ gas-cooled reactors and the Brayton cycle [3] to satisfy the requirements of small size, light weight, and simple layout. Furthermore, an appropriate working fluid must be selected to achieve the desired objectives. Incorporating a certain amount of xenon in a helium working fluid can significantly enhance its density and compressibility [6], thus addressing the disadvantages of helium while satisfying the aforementioned requirements. Consequently, gas-cooled reactors with direct cooling and closed helium-xenon Brayton cycles have been investigated extensively for the development of micronuclear power sources.

To satisfy the objectives mentioned above, the molar concentration of xenon in a helium–xenon gas mixture is

typically set between 8.6% and 30.0%. Within this range, the Prandtl number ( $Pr$ ) of the mixture is typically between 0.16 and 0.30 [7]. Based on reported data, the  $Pr$  range of the helium–xenon gas mixture is lower than that of typical gases such as air, hydrogen, and helium [8] but higher than those of liquid metals such as sodium [9] and lead–bismuth eutectic [10]. This unique  $Pr$  range endows the helium–xenon gas mixture with convective heat transfer characteristics that are distinct from those of the aforementioned fluids. Furthermore, in the core flow channel under conditions of high speed, high power, and nonuniform power distribution, the gas properties and structure of the thermal boundary layer undergo significant changes, which consequently affect the convective heat transfer. The preceding discussion clarifies that investigations into the convective heat transfer characteristics of a helium–xenon gas mixture in an intricate core environment is one of the primary areas of research pertaining to the thermal hydraulics of helium–xenon cooled microreactors.

Numerous significant findings regarding the heat transfer characteristics of helium–xenon gas mixtures have been published. In terms of experiments, Taylor et al. [11] examined the heat transfer properties of mixed gases, including helium–xenon gas mixtures, in a uniformly heated circular tube and assessed the feasibility of several typically used heat transfer correlations. To examine the convective heat transfer characteristics of helium–xenon gas mixtures with various channel geometries, Nakoryakov et al. [12–16] investigated the flow and heat transfer properties of a mixture in uniformly heated circular and triangular channels, as well as in circular-triangular transition regions. To achieve the actual geometric structure of a core, Makarov et al. [17] conducted experimental and numerical studies on the heat transfer process of a helium–xenon gas mixture in a thin-walled quasi-triangular pipe, which is suitable for densely packed fuel elements in the core. They analyzed the effects of channel geometry modifications and boundary layer development on the Nusselt number ( $Nu$ ) and discussed the significant decrease in wall temperature at the exit of the quasi-triangular reign and its underlying causes. In addition, Qin et al. [18] examined the convective heat transfer of helium–xenon gas mixtures in a uniformly heated vertical circular tube. They developed a more accurate  $Nu$  correlation and identified an applicable range.

Meanwhile, in terms of simulation, Vitovsky et al. [19] and Lushchik et al. [20] conducted researches on the flow and heat transfer properties of helium–xenon gas mixtures in a uniformly heated small-diameter (5.5 mm) tube. They proposed a method using the mass-average recovery temperature as the characteristic flow temperature, which extended the applicability range of the Dittus–Boelter correlation. In contrast to the approach of Vitovsky et al., Zhou et al. validated the existing turbulent  $Pr$  [7] and  $Nu$  correlations

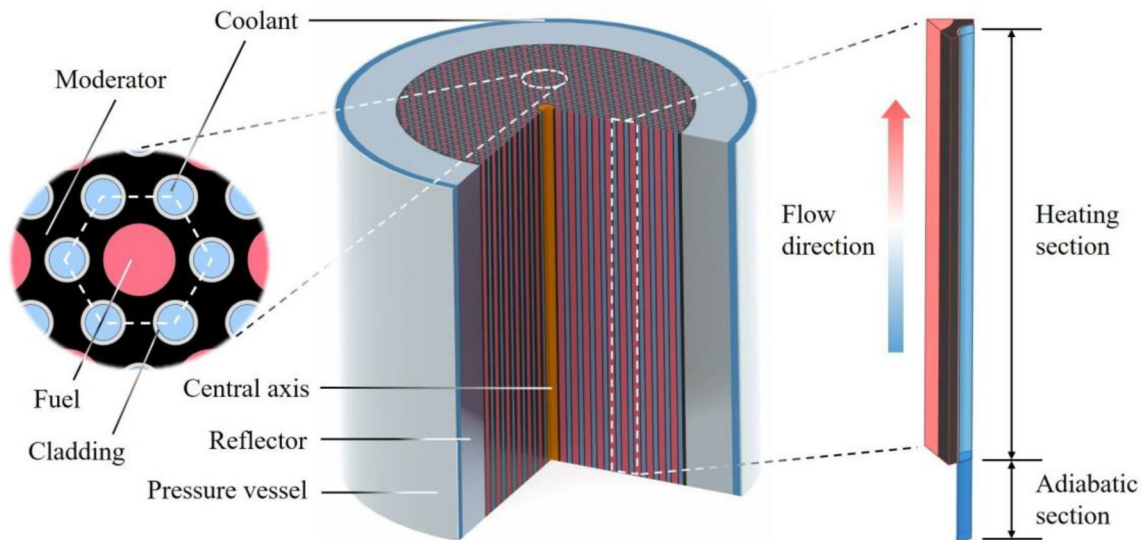


Fig. 1 (Color online) Longitudinal cross-sectional view of the core

Table 1 Geometric parameters of the model

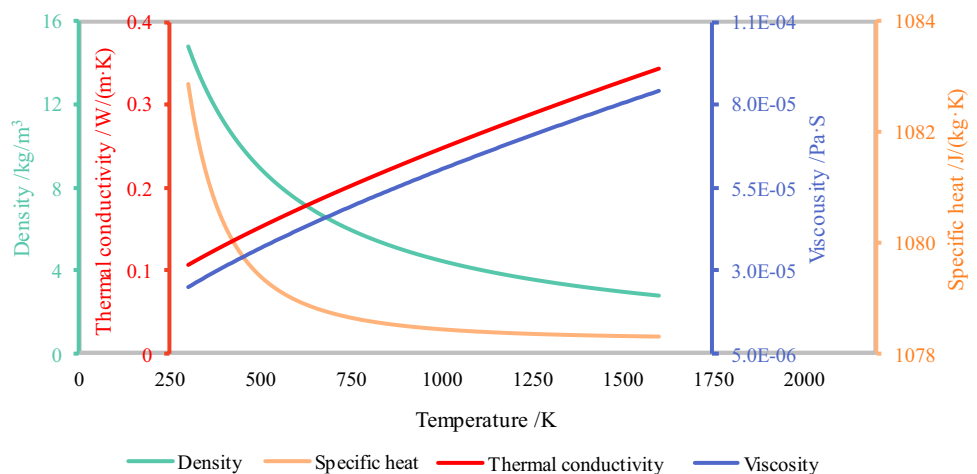
Parameter	Value (mm)
Diameter of fuel	15.0
Inner diameter of coolant channel	8.0
Thickness of cladding	0.5
Pitch	15.0
Length of coolant channel	1000

[21] and proposed new correlations with higher accuracy based on numerical simulations and theoretical derivations. Additionally, researchers have performed numerical simulations to investigate the heat transfer characteristics of helium–xenon gas mixtures in various channel types, including trilobe channels [22], annular channels, narrow rectangular channels [23], wire-wrapped annular channels [24],

and channels with internal vortex generators [25]. Additionally, to simulate the actual operating conditions of a nuclear reactor more accurately, Meng et al. [26] developed a 1/12-scale model of a helium–xenon cooled space reactor core and investigated the effects of bypass vessel cooling, surface radiation, flow channel blockage, and fuel rods on the heat transfer characteristics of the core.

The main objective of most relevant experimental and simulation studies is to establish the  $Nu$  correlation, which serves as a critical foundation for the development of multiphysical coupling [27, 28] and system analysis [29, 30] codes for nuclear reactors. However, these studies are based on the fundamental assumption of sufficiently developed temperature and flow fields. Nevertheless, in actual reactors, the power distribution is nonuniform, and the axial power distribution approximates a cosine function [31, 32]. Consequently, the thermal boundary layer inside the channel

Fig. 2 (Color online) Properties of the helium–xenon gas mixture over the operation temperature



cannot easily reach a fully developed state [33], thereby affecting the applicability of the  $Nu$  correlation in the core channels. To investigate the effect of the thermal boundary layer evolution on heat transfer, Sparrow et al. [34] derived a correlation for the axial  $Nu$  distribution of channels under uniform heat flux conditions, including the entrance region. The accuracy of the correlation was verified by comparing it with experimental results. Siegel et al. [35] expanded Sparrow's study and derived a relationship between the variation in the wall-to-bulk fluid temperature difference and the axial position under an arbitrary axial wall heat flux. Based on the studies of Sparrow and Siegel, researchers derived and validated relationships for the axial distribution of  $Nu$  under various conditions, including parallel plates [36], laminar flow [37], and a few simple heat flux distributions [38].

Clearly, investigations into the heat transfer characteristics of helium–xenon gas mixtures under nonuniform power distribution conditions are insufficient. Consequently, studies that investigate the effects of key operational parameters, such as power, flow velocity, and temperature, on the heat transfer characteristics under a nonuniform power distribution are few. Moreover, the applicability of the relevant conclusions in a nonuniform power distribution environment requires further verification.

Regarding the derivation of the  $Nu$  correlation, the correlation for the axial  $Nu$  distribution is inadequate when the axial power distribution reflects a cosine function and the power density at both the inlet and outlet positions is zero. For microreactors, the volume, mass, and complexity of the system should be reduced by eliminating the axial reflector, thereby resulting in an axial power distribution that conforms to the aforementioned conditions. Furthermore, additional studies are warranted to evaluate the applicability of Sparrow's method to the turbulent heat transfer of low  $Pr$  gases in a core environment.

In this study, computational fluid dynamics (CFD) methods are employed to examine the convective heat transfer properties of a helium–xenon gas mixture in a cylindrical coolant channel located within the core of the Small Innovative helium–xenon cooled MOBILE Nuclear power System (SIMONS) [39]. A three-dimensional multiregion conjugated heat transfer model is developed for one-third of the coolant channel. Based on this model, analyses are

performed to investigate the effects of various factors on  $Nu$ , including the axial power and distribution, inlet temperature and velocity, and outlet pressure. Subsequently, a theoretical correlation is derived for the axial  $Nu$  distribution in the channel, under the assumption of a cosine distribution for the axial power. Using the numerical simulation results, the unknown coefficients in the correlation are determined and a semi-empirical relationship is developed for the axial  $Nu$  distribution. Subsequently, the accuracy of the semi-empirical correlation is tested and compared with those of several existing correlations. Finally, a segmented correlation with higher accuracy is obtained by combining the semi-empirical correlation with another correlation.

## 2 Model and method

### 2.1 Geometry model

The SIMONS energy conversion system is based on a closed Brayton cycle, where the core serves as the heat source. The core was designed with a solid structure to achieve system miniaturization. Figure 1 shows a schematic illustration of the core. The solid core comprised staggered coolant channels and fuel rods. The nuclear fuel used was uranium carbide, the moderator was graphite, and the cladding was composed of a titanium zirconium molybdenum (Mo-TZM) alloy.

In Fig. 1, the dashed hexagonal line on the left represents a radially repeatable element located in the core. Because this element exhibits radial symmetry, a radial 1/6 structure was utilized for modeling. The details of the constructed geometric model are shown on the right side of Fig. 1. This model comprised solid regions for the fuel, moderator, and cladding, whereas the coolant channel was represented by a fluid region.

Under normal operating conditions, the low-temperature helium–xenon gas mixture enters the solid core from the channel inlet at the bottom of the core, is driven by the compressor, absorbs the heat released by the nuclear fuel, and flows out from the outlet at the top of the core. An adiabatic section is incorporated before the inlet to achieve a fully developed flow velocity distribution at the inlet of the heating section. The geometric parameters of the model are listed in Table 1.

### 2.2 Thermophysical properties

For helium–xenon cooled microreactors that utilize a closed Brayton cycle, the operating pressure of the helium–xenon gas mixture is typically approximately 2 MPa, and the operating temperature is between 400 and 1300 K [21]. To balance the thermal power, efficiency, miniaturization, and

**Table 2** Physical properties of materials

Region	Material	Density (kg/m <sup>3</sup> )	Thermal conductivity (W/(m·K))	Specific heat (J/(kg·K))
Fuel	UC	13,630.0	25.3	200.0
Moderator	Graphite	1850.0	70.0	1835.0
Cladding	Mo-TZM	10,220.0	118.0	255.0

**Table 3** Summary of boundary conditions for all operating conditions

Run no.	Power		Inlet		Outlet pressure (MPa)
	Distribution	Value (W)	Temperature (K)	Velocity (m/s)	
S	Cosine	3289.5	955.0	121.9	1.9
D1	Reflector at inlet	3289.5	955.0	121.9	1.9
D2	Reflector at outlet				
D3	Reflector at in & outlet				
D4	Uniform				
Q1	Cosine	822.4	955.0	121.9	1.9
Q2		1644.8			
Q3		2467.1			
Q4		4111.9			
T1	Cosine	3289.5	895.5	121.9	1.9
T2			945.3		
T3			1044.8		
T4			1094.5		
U1	Cosine	3289.5	955.0	91.4	1.9
U2				106.7	
U3				137.1	
U4				152.4	
P1	Cosine	3289.5	955.0	121.9	1.4
P2					1.7
P3					2.1
P4					2.4
UQ1	Cosine	2399.4	955.0	91.4	1.9
UQ2		2884.7		106.7	
UQ3		3694.3		137.1	
UQ4		4351.6		152.4	

lightweight requirements of the system, a helium–xenon gas mixture with a xenon volume fraction of 12% was selected as the working medium for the cycle.

The temperature-dependent properties of the mixture at a pressure of 1.9 MPa are shown in Fig. 2. Physical

properties, such as specific heat, thermal conductivity, and viscosity, are introduced into the CFD software using polynomials that are dependent only on temperature. Density was calculated using the ideal gas equation of state. The

**Fig. 3** (Color online) Schematic diagram of Taylor’s experimental section

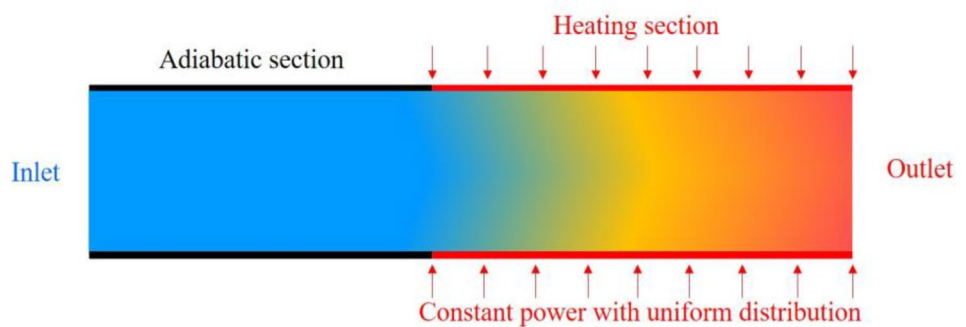


**Table 4** Parameter settings of Taylor’s experiments

Run no.	$M$ (g/mol)	$Pr$	$Re$	$T_{in}$ (K)	$P_{out}$ (Pa)	Heat flux ( $W/m^2$ )
689H	83.8	0.25	52,350–87,373	295.5	481,257	96,326
715H	14.5	0.30	19,485–34,042	303.0	807,381	296,622

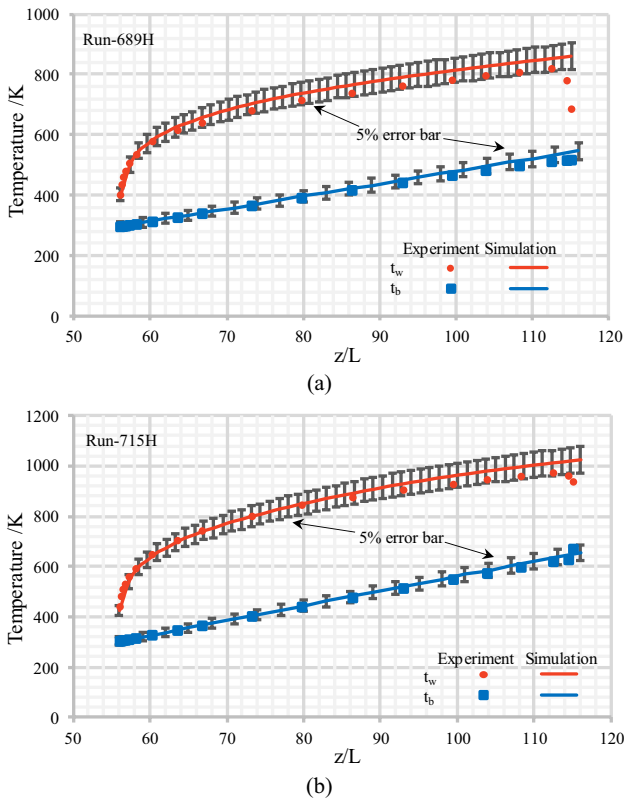


**Fig. 4** (Color online) Comparison between simulation and experimental results. **a** Run-689H; **b** Run-715H

physical properties of the solid regions were simplified to constants, as listed in Table 2.

### 2.3 Numerical models

This study employs the widely utilized CFD software STAR-CCM+ to conduct numerical simulations of flow and heat transfer in nuclear power systems [40, 41]. To balance computational time and resources, the Reynolds-averaged Navier–Stokes method was employed to accommodate turbulence fluctuation terms. A turbulence model was introduced to solve the Navier–Stokes equations. Currently,  $k$ -epsilon and shear stress transfer (SST)  $k$ -omega models are widely used in high Reynolds number ( $Re$ ) calculations. The SST  $k$ -omega model has been utilized in related studies [21, 22, 42] and yielded satisfactory results; thus, it was employed in this study. To enhance

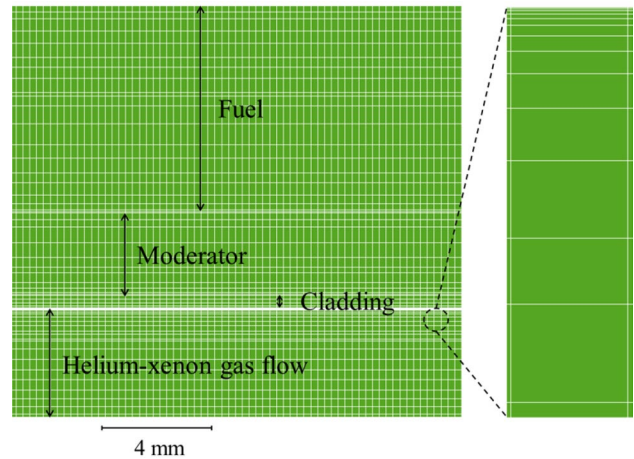


**Fig. 5** (Color online) Detailed grid view of the core flow channel model

the accuracy and convergence speed, an implicit coupling solver was employed for both the fluid and solid regions.

$Pr_t$  is a dimensionless parameter which affects the turbulent thermal conductivity. As mentioned previously, the helium–xenon mixture used in this study is a low  $Pr$  fluid that possesses properties distinct from those of conventional fluids. A study [7] showed that the  $Pr_t$  model developed by Kays [42] can be used to accurately calculate the  $Pr_t$  of a helium–xenon gas mixture, as expressed in Eq. 1.

$$Pr_t = \left\{ \frac{1}{2Pr_{t,b}} + CPe_t \sqrt{\frac{1}{Pr_{t,b}}} - (CPr_t)^2 \left[ 1 - \exp\left(-\frac{1}{CPr_t \sqrt{Pr_{t,b}}}\right) \right] \right\}^{-1}, \quad (1)$$

$$Pe_t = \frac{Pr \rho \epsilon_m}{\mu}, \quad (2)$$

where  $Pr_{t,b}$  is the  $Pr_t$  of the bulk region (0.85),  $C$  is a constant (0.3), and  $Pe_t$  is the turbulent Peclet number calculated using Eq. 2. Under the conditions investigated, the temperature did not significantly affect  $Pr$ .

Using  $Nu$  as a metric to quantify the degree of convective heat transfer is a widely recognized practice.  $Nu$  is expressed in Eq. 3 as follows:

$$Nu = \frac{Lh}{k}, \quad (3)$$

where  $h$  is the convection heat transfer coefficient, which is expressed as shown in Eq. 4:

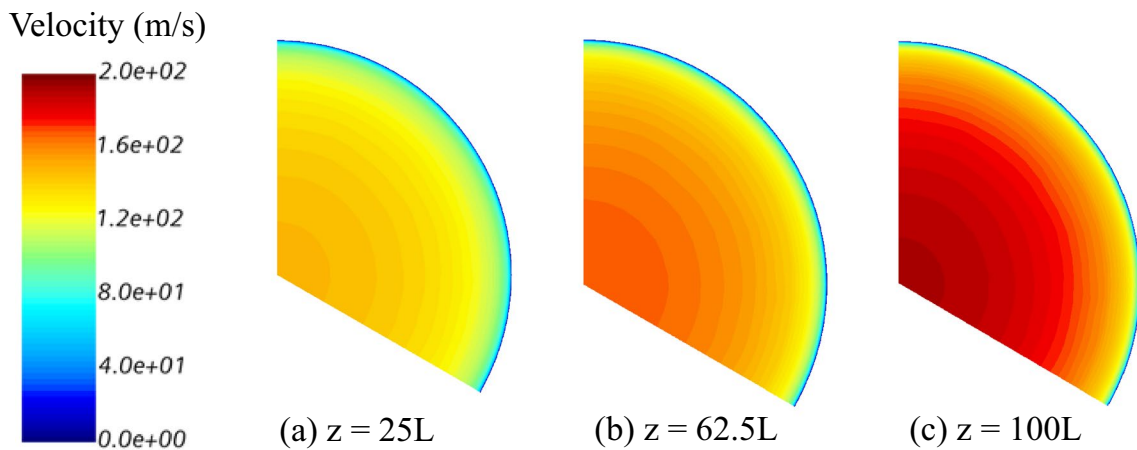


Fig. 6 (Color online) Flow velocity distribution at different axial positions

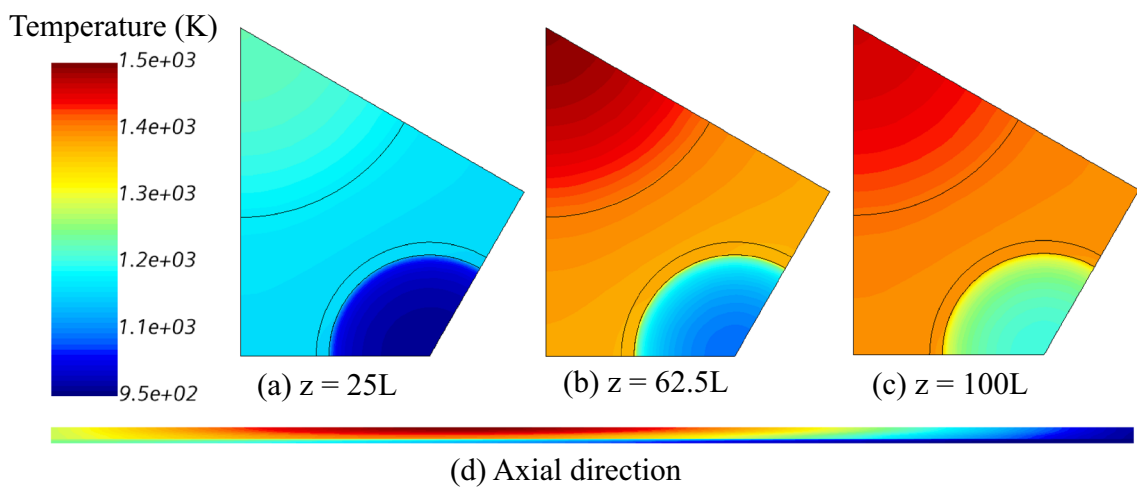


Fig. 7 Temperature distribution in solid and fluid regions

$$h = \frac{q}{t_w - t_b} \tag{4}$$

Here,  $t_b$  is the bulk temperature, which can be calculated using Eq. 5 as follows:

$$t_b = \frac{\int C_p \rho u t dA}{m C_p} \tag{5}$$

### 3 Simulation results

A series of numerical simulations are required to achieve a comprehensive understanding into the flow and heat transfer characteristics of helium–xenon mixtures in the core environment. In the simulation, the channel inlet was modeled as a velocity inlet, whereas the outlet was

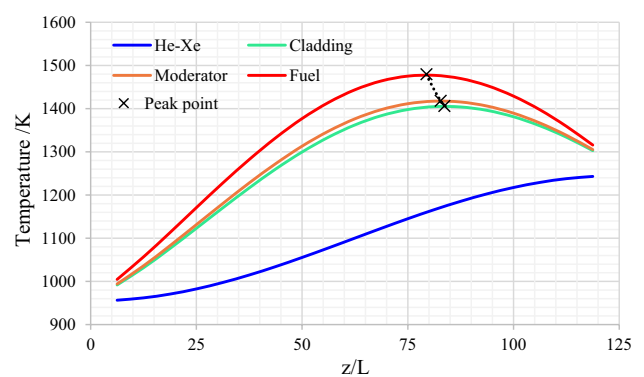


Fig. 8 (Color online) Axial distribution of radial mean temperature in different regions

modeled as a pressure outlet. Additionally, the bottom and top surfaces of the solid region were regarded as adiabatic, and the axial cross-sections of both the fluid and

solid regions were assumed to be symmetrical. The fuel region was regarded as a volumetric heat source. In addition, owing to the use of a helium–xenon gas mixture and metallic cladding, the effects of heat transfer deterioration and power shift resulting from fouling deposition were not considered in the calculations [44, 45].

Nineteen data measurement planes were uniformly distributed along the axial direction of the flow channel. Each measurement plane was positioned at a distance of 0.05 m from one another. No data measurement planes were positioned at the flow channel inlet or outlet. This is because the wall heat flux at these two positions was significantly lower than that at other locations within the channel. Consequently, including these positions in the analysis would yield unrepresentative results and extreme variations in  $Nu$ . Such variations are not conducive to subsequent analyses or interpretations.

To investigate the variables that affect convective heat transfer and quantify their respective magnitudes of influence, a sensitivity analysis was performed under five distinct boundary conditions. The operating conditions of the study are presented in Table 3, where Run-S was considered as the standard operating condition.

### 3.1 Model validation

The model was validated by comparing the simulation and experimental results of Taylor et al. [11]. A schematic diagram of the experimental setup is shown in Fig. 3; the adiabatic and heating sections of the tube were 328.72 and 352.20 mm long, respectively, and the inner diameter of the tube was 5.87 mm.

To verify the simulation results, data from two runs were selected: Run-689H, which featured gas  $Pr$  and  $Re$  ranges closest to those in the current study; and Run-715H, which featured gas mole mass and temperature ranges closest to those in the current study. The turbulence model, solver, and  $Pr_t$  model used in the simulation were consistent with those

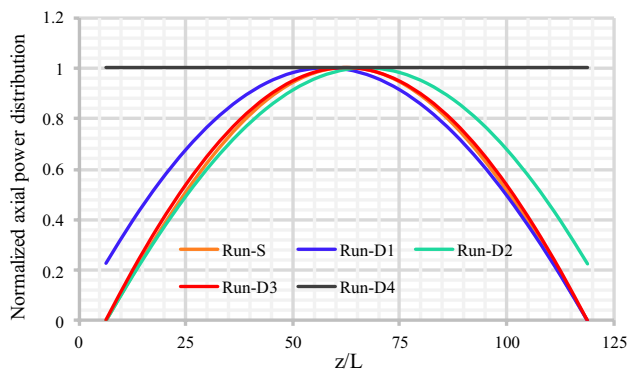


Fig. 9 (Color online) Power distribution under different conditions

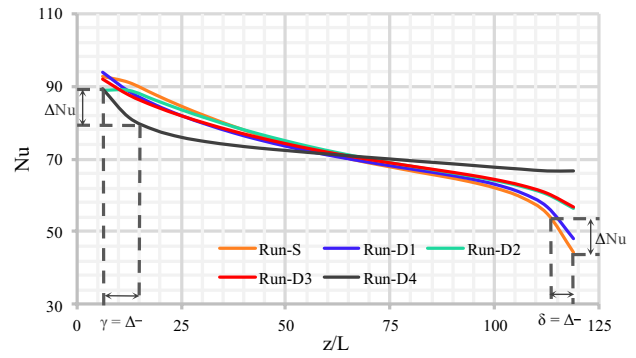


Fig. 10 (Color online) Axial  $Nu$  distribution under different axial power distributions

described in Sect. 2. The boundary conditions for the two experiments are listed in Table 4, and a comparison of the simulation and experimental results is presented in Fig. 4.

As shown in Fig. 4, both experiments showed a significant decrease in the wall temperatures near the outlet, which is likely due to the axial heat conduction of the tube wall [22]. Under two separate operating conditions, the relative error between the experimental and simulated data was less than 5%. The simulated Run-689H and Run-715H exhibited maximum relative errors of 4.4% and 4.2%, respectively, whereas their average relative errors were 2.8% and 1.9%, respectively, except for two points situated near the outlet.

In addition, both the aforementioned model and the core channel model satisfied the criteria for grid independence. Figure 5 illustrates the grid partitioning of the core channel model along the axial direction. The grid was refined in the vicinity of the wall within the fluid region to ensure that the center of the first layer of the grid cells was positioned within the viscous sublayer.

### 3.2 Flow and temperature field of standard condition

To analyze the flow and heat transfer characteristics of the helium–xenon gas mixture in the core environment, one must examine the velocity and temperature distributions in

Table 5 Characteristic parameters under different axial power distributions

Run no.	$Nu$			$\gamma$ (z/L)	$\delta$ (z/L)
	Maximum	Minimum	Average		
S	92.68	44.20	71.73	16.76	4.22
D1	93.74	48.13	71.59	9.57	5.16
D2	88.92	56.34	72.96	23.78	17.20
D3	92.04	56.60	72.62	11.97	17.34
D4	89.34	66.88	72.59	5.81	82.96

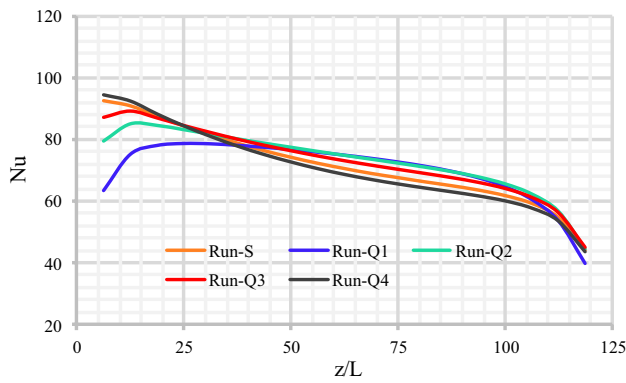


**Fig. 11** (Color online) Axial  $Nu$  distribution under different power values

**Table 6** Characteristic parameters under different power values

Run no.	$Nu$			$\delta (z/L)$
	Maximum	Minimum	Average	
S	92.68	44.20	71.73	4.22
Q1	78.52	39.97	69.96	3.18
Q2	85.10	44.34	72.87	3.71
Q3	89.03	44.96	72.70	4.04
Q4	94.22	43.60	70.51	4.44

both the flow channel and the surrounding solid region. Figure 6 shows the radial velocity distribution at various axial positions within the flow channel.

Based on Fig. 6, the fluid flowed gradually from the inlet to the outlet and the gas expanded owing to the heating of the fuel elements, thus resulting in a velocity increase. Under normal operating conditions, the maximum local velocity in the flow channel reached approximately 199 m/s, which corresponded to approximately 20% of the local speed of sound. Additionally, as shown in Fig. 6, a significant velocity gradient appeared in the near-wall region. This is attributed to the fluid experiencing resistance from the adjacent wall, which resulted in a lower velocity compared with that at the mainstream flow region.

Figure 7 presents the temperature distribution in both the flow channel and the surrounding solid region. Figures 7(a)–(c) illustrate the radial temperature distributions at different axial positions, whereas Fig. 7(d) depicts the axial temperature distributions of all four regions.

Based on Fig. 7, the fuel region demonstrates unsatisfactory thermal uniformity, primarily because of its relatively low thermal conductivity. By contrast, the moderator and cladding regions exhibited better thermal uniformity. Additionally, a significant temperature gradient was observed in the near-wall region of the fluid, where the cladding

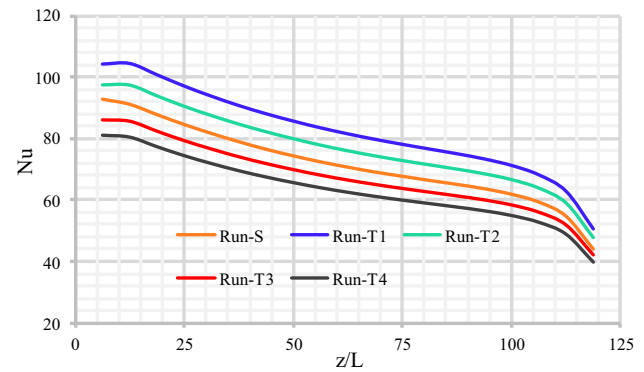


**Fig. 12** (Color online) Axial  $Nu$  distribution under different inlet temperatures

**Table 7** Characteristic parameters under different inlet temperatures

Run no.	$Nu$			$\gamma (z/L)$	$\delta (z/L)$
	Maximum	Minimum	Average		
S	92.68	44.20	71.73	16.76	4.22
T1	104.67	50.75	82.61	20.79	4.20
T2	97.48	47.52	76.85	20.13	4.24
T3	85.90	41.90	67.25	18.68	4.31
T4	81.01	39.55	63.27	17.99	4.33

temperature significantly exceeded that of the helium–xenon gas mixture.

The axial distributions of the radial average temperature for each solid and fluid region is illustrated in Fig. 8. As shown, the temperature peak points of the three solid regions were located in the latter half of the flow channel. Furthermore, the proximity of a region to the fluid region corresponded to the proximity of its peak temperature point to the outlet. This phenomenon arises because of the gradual increase in fluid temperature along the flow channel and the cosine distribution of power in the axial direction. Additionally, the helium–xenon gas mixture experienced a rapid temperature increase in the middle of the flow channel and a slower temperature increase at both ends, which is attributable to the cosine distribution of the axial power.

### 3.3 Effects of operating parameters on $Nu$

#### 3.3.1 Power distribution

To render the current study more applicable to practical operating conditions, the axial power distribution for four different operating conditions, namely Run-D1 to Run-D4, was designed based on the actual configuration of the axial reflector in the reactor core and previous heat transfer experiments. Table 3 presents the boundary conditions for each

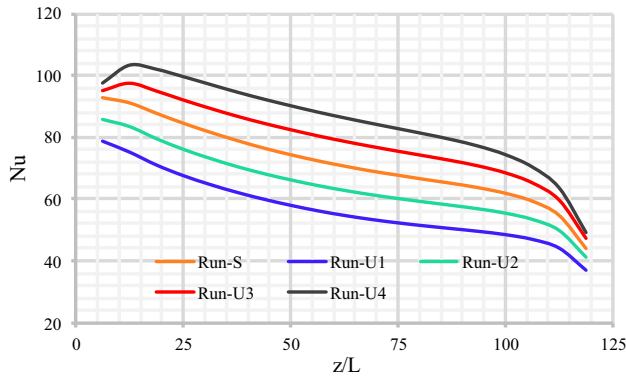


**Fig. 13** (Color online) Axial  $Nu$  distribution under different inlet velocities

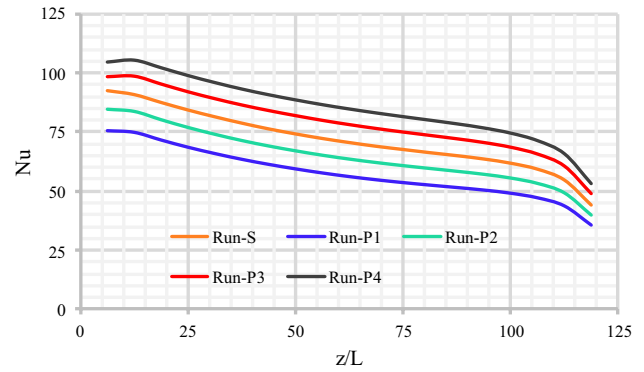


**Fig. 14** (Color online) Axial  $Nu$  distribution under different outlet pressures

**Table 8** Characteristic parameters under different inlet velocities

Run no.	$Nu$			$\gamma$ ( $z/L$ )	$\delta$ ( $z/L$ )
	Maximum	Minimum	Average		
S	92.68	44.20	71.73	16.76	4.22
U1	78.65	36.76	56.80	9.47	4.94
U2	85.89	40.95	64.46	12.85	4.62
U3	97.63	47.25	78.62	30.22	3.95
U4	103.29	49.14	84.89	47.34	3.67

**Table 9** Characteristic parameters under different outlet pressures

Run no.	$Nu$			$\gamma$ ( $z/L$ )	$\delta$ ( $z/L$ )
	Maximum	Minimum	Average		
S	92.68	44.20	71.73	16.76	4.22
P1	75.71	35.39	57.50	16.10	4.38
P2	84.55	39.93	64.81	16.48	4.32
P3	98.32	48.89	78.51	21.99	4.22
P4	105.38	53.03	84.96	24.58	4.18

operating condition and Fig. 9 shows the normalized power distributions.

Figure 9 shows that the addition of the reflector significantly increased the normalized wall heat flux density near the inlet of Run-D1 and outlet of Run-D2. Additionally, although the normalized wall heat flux distributions for Run-D3 and Run-S were almost identical, the former demonstrated a significantly higher wall heat flux density near the inlet and outlet of the channel than the latter.

Figure 10 shows the axial distribution of  $Nu$  under different operating conditions. Table 5 lists the heat transfer characteristic parameters for each operating condition. To analyze the effects of different factors on the axial change rate of  $Nu$ ,  $\Delta Nu$  was defined as 10% of the average  $Nu$  obtained in each run. Additionally, two dimensionless distances were introduced:  $\gamma$ , which represents the distance required downstream of the first measuring point to observe a decrease of  $\Delta Nu$ , and  $\delta$ , which represents the distance required upstream of the last measuring point to observe an increase of  $\Delta Nu$ . These values are also marked in Fig. 10.

As shown in Fig. 10,  $Nu$  decreased along the flow direction, and the decreasing trend was consistent across all operating conditions, except for the case of uniform power distribution. In the case of uniform power distribution,  $Nu$  decreased significantly near the inlet, whereas the rate of decrease at other positions decelerated considerably. Similar

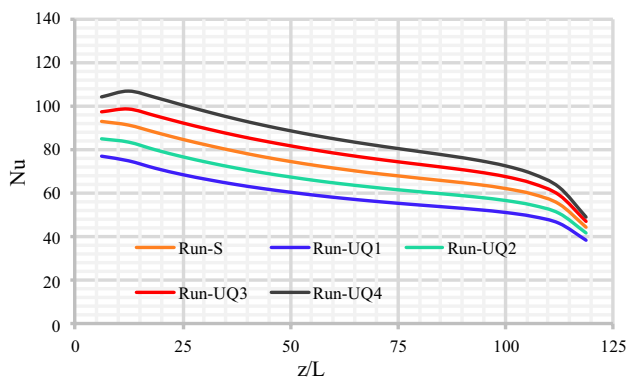
phenomena were reported by Sparrow [34] and Vitovsky [16].

Table 5 indicates that the addition of a reflector at the inlet increased the axial decline rate of  $Nu$  near the inlet. By contrast, incorporating a reflector at the outlet can reduce the axial decline rate of  $Nu$ , thus improving  $Nu$  near the outlet and contributing positively to heat transfer. Hence, incorporating reflectors near the core outlet can potentially provide supplementary thermal safety margins for the core. However, in the case of microreactors, one must scrutinize the tradeoff between the benefits of enhanced thermal safety and the associated increase in core volume and weight resulting from the addition of reflectors.

### 3.3.2 Power value

To investigate the effect of power on the channel heat transfer, four sets of operating conditions, namely Run-Q1 to Run-Q4, with different power values were designed, and their  $Nu$  distributions were compared with those of Run-S. The boundary conditions for each operating condition are listed in Table 3. The axial distribution of  $Nu$  and the heat transfer characteristic parameters for each operating condition are presented in Fig. 11 and Table 6, respectively.

As shown in Fig. 7, power exerted a positive effect on  $Nu$  near the inlet. However, as the power increased, the effect



**Fig. 15** (Color online) Axial  $Nu$  distribution under different inlet velocities with fixed inlet/outlet temperatures

**Table 10** Characteristic parameters under different outlet pressures with fixed inlet/outlet temperatures

Run no.	$Nu$			$\gamma(z/L)$	$\delta(z/L)$
	Maximum	Minimum	Average		
S	92.68	44.20	71.73	16.76	4.22
UQ1	76.70	38.19	58.60	13.20	4.72
UQ2	84.63	41.49	65.14	15.41	4.52
UQ3	98.67	47.10	78.25	24.55	4.04
UQ4	106.78	49.19	84.43	27.86	3.87

weakened. Furthermore, the  $Nu$  in the axial middle section of the channel decreased gradually as the total power increased. This can be attributed to the lower fluid temperature at lower power levels, which results in a lower viscosity and higher  $Re$  under similar flow velocities. Based on the preceding discussion, one can infer that under certain circumstances, such as low-power operation or transient conditions, the phenomenon in which the cladding temperature at the reactor inlet exceeds the expected value must be considered.

In terms of the rate of change of  $Nu$ , the distribution of  $Nu$  under certain working conditions exhibited a significant nonlinear trend. Hence, only the rate of change of  $Nu$  near the outlet is presented in Table 6. As shown in the table, the power level did not significantly affect the rate of decrease in  $Nu$  near the outlet.

### 3.3.3 Inlet temperature

Operating conditions Run-T1 to Run-T4 were imposed to investigate the effect of the inlet temperature on the axial

distribution of  $Nu$ . The boundary conditions, axial distribution of  $Nu$ , and heat transfer characteristic parameters for each case are presented in Table 3, Fig. 12, and Table 7, respectively.

Based on the results presented in Fig. 12 and Table 7, as the inlet temperature decreased, the overall  $Nu$  in the channel increased, and the rate of increase in the average  $Nu$  was approximately  $-0.094/K$ . This phenomenon can be attributed to a decrease in the inlet temperature, which resulted to an increase in the fluid density and a decrease in the viscosity, thus causing an increase in  $Re$ .

Although reducing the inlet temperature of the core can improve the overall heat transfer efficiency, it may decrease the outlet temperature, which consequently affects the thermal-electric conversion efficiency of the system.

As shown in Table 7, the effect of the inlet temperature on the rate of change of  $Nu$  near the inlet and outlet was insignificant.

### 3.3.4 Inlet velocity

The results of the simulations for Runs-U1 to Run-U4 can be used to investigate the effect of the flow velocity on the axial distribution of  $Nu$  based on a comparison with the results of Run-S. The boundary conditions, axial distribution of  $Nu$ , and heat transfer characteristic parameters for each case are presented in Table 3, Fig. 13, and Table 8, respectively.

Based on Fig. 13 and Table 8,  $Nu$  increased with the flow velocity in the axial middle section of the channel at an average increase rate of  $0.468\text{ s/m}$ . This is because an increase in flow velocity improves the mass flow rate and reduces the average fluid temperature, thus resulting in an overall increase in  $Re$ .

Furthermore, as the velocity increased, the positive effect of high velocity on  $Nu$  near the inlet weakened gradually, thus resulting in a lower axial decrease rate of  $Nu$  near the inlet. Additionally, the effect of the inlet velocity on the axial change rate of  $Nu$  near the outlet was insignificant.

Based on the preceding discussion, one can infer that increasing the inlet flow velocity can enhance the overall heat transfer efficiency of the core. However, the rate of improvement in the heat transfer efficiency at the inlet may not be as significant as that in other regions. Consequently, this increase in the flow velocity can result in higher cladding temperatures at the inlet than anticipated.

### 3.3.5 Outlet pressure

The results of Run-P1 to Run-P4 were compared with those of Run-S to investigate the effect of the outlet pressure on the axial distribution of  $Nu$ . During the modification of the outlet pressure, the physical properties of the helium–xenon gas mixture were adjusted accordingly. The boundary

conditions, axial distribution of  $Nu$ , and heat transfer characteristic parameters for each case are presented in Table 3, Fig. 14, and Table 9, respectively.

As shown in Fig. 14 and Table 9,  $Nu$  increased with the outlet pressure, and the average  $Nu$  increased at a rate of approximately 0.031/kPa. The increase in  $Nu$  can be attributed to the increase in fluid density caused by the increase in pressure, which results in an overall increase in  $Re$  and an improved heat transfer performance.

Caution must be exercised when increasing the inlet pressure to enhance the heat transfer efficiency in the core because it can affect the volume and mass of the compressor, thus potentially affecting the flexibility of the micronuclear reactor power source.

As shown in Table 9, the effect of the outlet pressure on the axial change rate of  $Nu$  near the inlet and outlet was insignificant.

### 3.3.6 Inlet velocity under fixed inlet and outlet temperatures

One approach to determine the operating range of a closed Brayton cycle nuclear power system is to vary the core power while maintaining a constant temperature increase in the core and then observe changes in parameters such as the system thermoelectric conversion efficiency. Using this method, operating conditions Run-UQ1 to Run-UQ4 were established by adjusting the total power to maintain a stable outlet temperature based on operating conditions Run-U1 to Run-U4. The simulation results of Run-UQ1 to Run-UQ4 were compared with those of Run-S to evaluate the effects of varying the total power. The boundary conditions, axial distribution of  $Nu$ , and heat transfer characteristic parameters for each case are presented in Table 3, Fig. 15, and Table 10, respectively.

As shown in Fig. 15,  $Nu$  increased with the inlet velocity, and the average  $Nu$  increased at a rate of approximately 0.431 s/m, which was lower than the result presented in Sect. 3.3.4.

As shown in Table 10, similar to the conclusion in Sect. 3.3.4, as the inlet velocity increased, the positive effect of the high velocity on  $Nu$  near the inlet gradually weakened. However, under the operating conditions investigated in this section, this weakening trend became less pronounced owing to the change in the power. Furthermore, the inlet velocity did not significantly affect the decreasing rate of  $Nu$  near the outlet.

## 4 Correlation for axial $Nu$ distribution

### 4.1 Theoretical derivation

To depict the axial variation in  $Nu$  in the channel in the core environment precisely, a theoretical framework that can capture the changing behavior of the thermal boundary layer is necessary. Sparrow et al. presented a theoretical derivation based on the theory of turbulent boundary layers and eddy viscosity. According to their theory, the wall-to-bulk temperature difference along the axial direction of a circuit channel under turbulent heat transfer conditions of forced convection with a uniform axial power distribution can be expressed as shown in Eq. 6 [34].

$$t_w - t_b = \frac{qL}{2k} \left\{ G(r_0^+) + \sum_{n=0}^{\infty} F_n \exp \left[ -\frac{4\beta_n^2 z}{Re L} \right] \right\}, \quad (6)$$

where  $G(r_0^+)$  denotes the dimensionless wall-to-bulk temperature difference in the fully developed temperature field;  $F_n$  is the coefficient of the series expansion of the wall temperature, which is a negative value that depends only on  $Re$ ,  $Pr$ , and  $G$ ;  $\beta_n^2$  is the eigenvalue and is related only to  $Re$  and  $Pr$ . The derivation of Eq. 6 is based on the following six assumptions:

- I. The fluid properties are constant.
- II. Compared with the radial heat diffusion, the axial diffusion of both molecular and turbulent heat is negligible.
- III. The mean value of the radial velocity is 0.
- IV. Viscous dissipation is negligible.
- V. The turbulence velocity distribution is fully developed throughout the channel.
- VI. The turbulent  $Pr$  can be approximated as 1.

This equation can be used to precisely calculate the distribution of the axial wall-to-bulk temperature difference, including that at the thermal entrance region. Additionally,  $G(r_0^+)$  can be expressed as

$$G(r_0^+) = - \sum_{n=0}^{\infty} F_n. \quad (7)$$

Based on Eq. 6, when  $z=0$  (i.e., at the entrance), the wall-to-bulk temperature difference is 0; when  $z=\infty$  (i.e., where the temperature is fully developed), the temperature difference is a constant.

For operational conditions with an arbitrary axial power distribution, the power distribution can be regarded as a combination of multiple power steps, with each power step affecting the downstream temperature distribution [35]. Based on Eq. 6, if no heat flux appears on the wall before

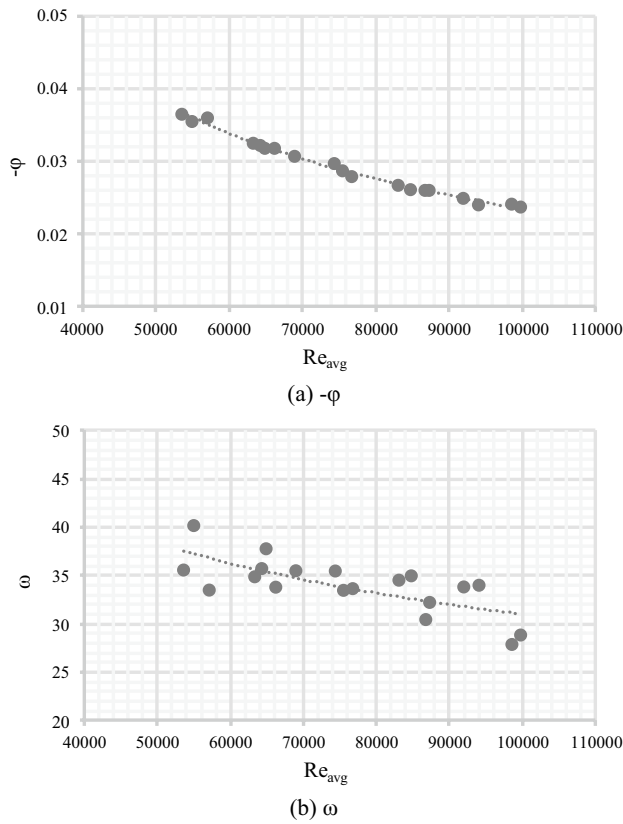


**Fig. 16** Relationship between the coefficients and average  $Re$  (dashed line represents the function graph of the fitted equation, and the average  $Re$  is within the range of  $5.3 \times 10^4$  to  $1 \times 10^5$ )

position  $z$  and a uniform heat flux of  $dq$  appears after  $z$ , then the temperature difference downstream  $\tilde{z}$  can be calculated as

$$t_w - t_b|_{\tilde{z}} = dq \cdot \frac{L}{2k} \left\{ G(r_0^+) + \sum_{n=0}^{\infty} F_n \exp \left[ -\frac{4\beta_n^2}{Re} \frac{\tilde{z} - z}{L} \right] \right\} \quad (z \leq \tilde{z}) \quad (8)$$

Integrating the equation above yields the following expression for the wall-to-bulk temperature difference at  $\tilde{z}$  under an arbitrary axial power distribution [35]:

$$t_w - t_b|_{\tilde{z}} = -\frac{2}{kRe} \sum_{n=0}^{\infty} F_n \beta_n^2 \int_0^{\tilde{z}} q(z) \exp \left[ -\frac{4\beta_n^2}{Re} \frac{\tilde{z} - z}{L} \right] dz. \quad (9)$$

Without axial reflectors, the axial power distribution in the core can be approximated using a cosine function as follows:

$$q(z) = \alpha \cos \left[ \pi \left( z - \frac{1}{2} \right) \right]. \quad (10)$$

After simplification, it can be expressed as

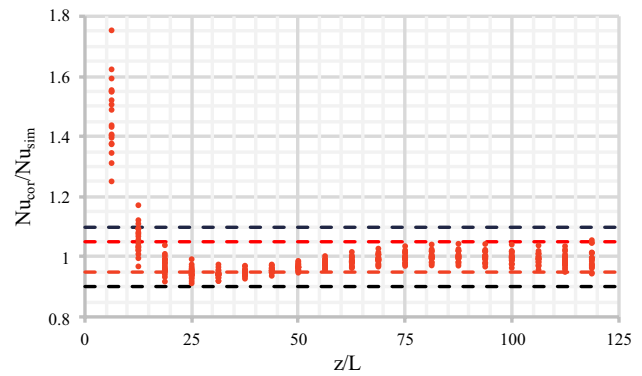


**Fig. 17** Comparison of calculations using Eq. 17 with simulation results (relative error within red and black dashed lines is less than 5% and 10%, respectively)

$$q(z) = \alpha \sin(\pi z). \quad (11)$$

By substituting Eq. 11 into Eq. 9, the equation for the wall-to-bulk temperature difference at  $\tilde{z}$  under a cosine power distribution can be obtained as follows:

$$t_w - t_b|_{\tilde{z}} = -\frac{2\alpha}{kRe} \sum_{n=0}^{\infty} F_n \beta_n^2 \frac{\int_0^{\tilde{z}} \sin(\pi z) \exp \left[ \frac{4\beta_n^2}{Re} \frac{z}{L} \right] dz}{\exp \left[ \frac{4\beta_n^2}{Re} \frac{\tilde{z}}{L} \right]}. \quad (12)$$

Let  $a_n = \frac{4\beta_n^2}{ReL}$ . Therefore, the temperature difference at  $\tilde{z}$  can be expressed as

$$t_w - t_b|_{\tilde{z}} = \frac{2\alpha}{kRe} \sum_{n=0}^{\infty} F_n \beta_n^2 \frac{\pi \cos(\pi \tilde{z}) - \frac{\pi}{\exp(a_n \tilde{z})} - a_n \sin(\pi \tilde{z})}{a_n^2 + \pi^2}. \quad (13)$$

The axial distribution of  $Nu^{-1}$  under the cosine power distribution is represented as shown in Eq. 14.

$$Nu^{-1} = \frac{t_w - t_b}{q(\tilde{z})} \frac{k}{L} = \frac{1}{2} \sum_{n=0}^{\infty} \frac{F_n a_n}{a_n^2 + \pi^2} \left\{ \pi \left[ \cot(\pi \tilde{z}) - \frac{1}{\sin(\pi \tilde{z}) \exp(a_n \tilde{z})} \right] - a_n \right\} \quad (14)$$

In Eq. 14, when  $\tilde{z}$  approaches 1 m from the left side, the following equation is satisfied.

$$\lim_{\tilde{z} \rightarrow 1^-} \left\{ \pi \left[ \cot(\pi \tilde{z}) - \frac{1}{\sin(\pi \tilde{z}) \exp(a_n \tilde{z})} \right] - a_n \right\} = -\infty \quad (15)$$

Thus, in the region near the channel outlet,  $Nu^{-1}$  approaches infinity, whereas  $Nu$  approaches zero ( $a_n > 0$ ),

**Table 11** Operating conditions to validate Eq. 17

Run no.	Power		Inlet		Outlet pressure (MPa)	
	Distribution	Value (W)	Temperature (K)	Velocity (m/s)	Temperature (K)	Velocity (m/s)
V1	Cosine	3289.5	1002.8	134.1	1.7	1.7
V2		3618.5	859.5	97.5	1.9	1.9
V3		2960.6	955.0	134.1	1.9	1.9
V4		3289.5	907.3	134.1	1.9	1.9

$F_n < 0$ ). As  $\tilde{z}$  approaches 0 m from the right side, it satisfies the following equation:

$$\lim_{\tilde{z} \rightarrow 0^+} \left\{ \pi \left[ \cot(\pi\tilde{z}) - \frac{1}{\sin(\pi\tilde{z})\exp(a_n\tilde{z})} \right] - a_n \right\} = 0. \quad (16)$$

Hence, near the inlet,  $Nu^{-1}$  approaches 0, whereas  $Nu$  approaches infinity.

As shown in Eq. 14,  $F_n$  and  $a_n$  are critical parameters that affect the  $Nu$ . In Sparrow and Siegel’s series of studies [34, 35], the values of  $F_n$  and  $a_n$  were obtained by solving the eigenvalue system of the Sturm–Liouville type, which is based on the six assumptions mentioned above. In this study, the high flow velocity of the helium–xenon gas mixture renders viscous dissipation a significant factor that affects the  $Nu$  distribution under certain operating conditions. Moreover, the gas is heated vigorously in the channel, thus causing changes in the physical properties and a pronounced acceleration effect. This renders it challenging to satisfy the conditions of constant properties and a fully developed turbulent velocity distribution. Therefore, the six assumptions mentioned earlier may not be entirely valid, whereas solving the eigenvalue equation to determine  $F_n$  and  $a_n$  may introduce a significant deviation.

In addition, coefficients  $F_n$  and  $a_n$  in Eq. 14 are related to the characteristic values, which result in an infinite number of unknown coefficients that must be determined, thereby rendering the equation impractical for engineering applications. To reduce the number of unknown coefficients,  $F_n$  and  $a_n$  in Eq. 14 were simplified as  $\varphi$  and  $\omega$ , respectively, and existing simulation data were used to determine the values of  $\varphi$  and  $\omega$  for various operating conditions. The subsequent analysis indicates that this simplification affected the accuracy of the relationship at a reasonable level. Hence, Eq. 14 can be simplified as follows:

$$Nu = 2 \frac{\omega^2 + \pi^2}{\varphi\omega} \left\{ \pi \left[ \cot(\pi\tilde{z}) - \frac{1}{\sin(\pi\tilde{z})\exp(\omega\tilde{z})} \right] - \omega \right\}^{-1}. \quad (17)$$

Using the MATLAB Genetic Algorithm Toolbox, the axial distribution of  $Nu$  for all operating conditions in Sect. 3, which presents axial power distributions in the form of a cosine function (excluding Run-Q1 and Run-Q2, which exhibited clear nonlinear trends), was fitted using Eq. 17. The variations in  $-\varphi$  and  $\omega$  with the average  $Re$  of each operating condition are presented in Fig. 16. The average  $Re$  of each condition was calculated as follows:

$$Re_{avg} = \frac{Re_{in} + Re_{out}}{2} = \frac{2m(\mu_{in} + \mu_{out})}{\pi L \mu_{in} \mu_{out}} \quad (18)$$

When  $Pr = 0.264$  and the average  $Re$  was between  $5.3 \times 10^4$  to  $1 \times 10^5$ , the relationship between  $\varphi$  and the

**Table 12** *Nu* correlations

Name	Range of <i>Re</i>	Range of <i>Pr</i>	Correlations
Dittus–Boelter	$Re > 10^4$	$0.7 < Pr < 160$	$Nu = 0.023Re^{0.8}Pr^{0.4}$
Churchill	$Re > 10^4$	$0.001 < Pr < 200$	$Nu = 6.3 + \frac{0.079Re\sqrt{f}Pr}{(1+Pr^{0.8})^{5/6}}$ $1/\sqrt{f} = 2.21\ln(Re/7)$
Kays	$Re > 10^4$	$0.5 < Pr < 1.0$	$Nu = 0.022Re^{0.8}Pr^{0.6}$
Pickett	$3.12 \times 10^4 < Re < 1.02 \times 10^5$	$0.42 < Pr < 0.49$	$Nu = 0.021Re^{0.8}Pr^e \left[ \left( \frac{t_w}{t_b} \right)^{-0.4} + \frac{0.85L}{z} \right]$ $e = 0.65$

average *Re*, as well as that between  $\omega$  and the average *Re*, were fitted using power functions. The results are expressed as shown in Eqs. 19 and 20.

$$\varphi = -90.72Re_{avg}^{-0.72} \tag{19}$$

$$\omega = 1075.65Re_{avg}^{-0.31} \tag{20}$$

Here, the *Nu* at any axial position  $\tilde{z}$  in the flow channel can be calculated conveniently using Eq. 17. In the following section,  $\tilde{z}$  is uniformly substituted with *z* in the relevant correlations to facilitate understanding.

### 4.2 Verification and analysis

As shown in Fig. 17, the axial *Nu* distribution calculated using Eq. 17 was compared with the simulation results for all the operating conditions listed in Table 3, where the axial power distribution was cosine (excluding Run-Q1 and Run-Q2).

As shown in Fig. 17, the most significant difference was indicated in the region near the inlet, with a maximum relative error of 75.3%, whereas the average relative error was approximately 5.2%. Approximately 94% of the data points showed a relative error within 10%, of which and 78% indicated a relative error within 5%. Moreover, in the latter half of the channel ( $z/L \geq 62.5$ ), almost all the data points showed a relative error within 5%.

Table 11 presents the boundary conditions of the four newly established cases, which are distinct from those in Table 3, used to assess the validity of Eq. 17.

Based on the calculations performed using Eq. 18, the average *Re* of conditions Run-V1 to V4 were approximately  $5.9 \times 10^4$ ,  $6.9 \times 10^4$ ,  $8.6 \times 10^4$ , and  $9.3 \times 10^4$ , respectively.

To evaluate the accuracy of Eq. 17, the calculation error and the errors of several existing and widely used

correlations were compared. Previous studies [11, 18, 21] showed that the Dittus–Boelter [46], Churchill [47], Kays [48], and Pickett [49] methods are more accurate for calculating the *Nu* of a helium–xenon gas mixture compared with other correlations. The expressions and applicabilities of the four relationships are listed in Table 12. The accuracies of the four methods above and Eq. 17 were compared, as shown in Fig. 18. Notably, the *Nu* values obtained from the correlations in Table 12 were calculated using the local *Re*, whereas used  $Re_{avg}$  was used in Eq. 17 for the calculations.

As shown in Fig. 18, Eq. 17 demonstrated high accuracy in most axial positions, with a lower relative error compared with the Dittus–Boelter, Churchill, Kays, and Pickett correlations. Most of the observations indicated a relative error of less than 10%, except for two points near the inlet. In the latter half of the duct, almost all data points indicated a relative deviation of less than 5%. Table 13 lists the maximum and average relative errors of each correlation for all the data points under the four operating conditions listed in Table 11.

As presented in Table 13, the Dittus–Boelter correlation showed the highest maximum and average relative errors among the five correlations, thus indicating that its predictive performance was the least ideal. However, the accuracy of Eq. 17 was the lowest, with only approximately one-half of the error indicated in the Pickett correlation, thus rendering it the most accurate among the five correlations. Furthermore, based on the calculation results for all four operating conditions, the Kays correlation yielded the most accurate prediction for the entrance area ( $z/L \leq 18.75$ ), with an average relative error of 4.5%. In the outlet area ( $z/L \geq 106.25$ ), Eq. 17 yielded the highest prediction accuracy, with an average relative error of 2.2%. The results above validated the theoretical derivation and confirmed the feasibility of Eq. 17 for turbulent heat transfer calculations in a helium–xenon gas mixture in a core environment.

Furthermore, Eq. 17 showed high accuracies for calculations near the outlet but exhibited low accuracy near the inlet, in

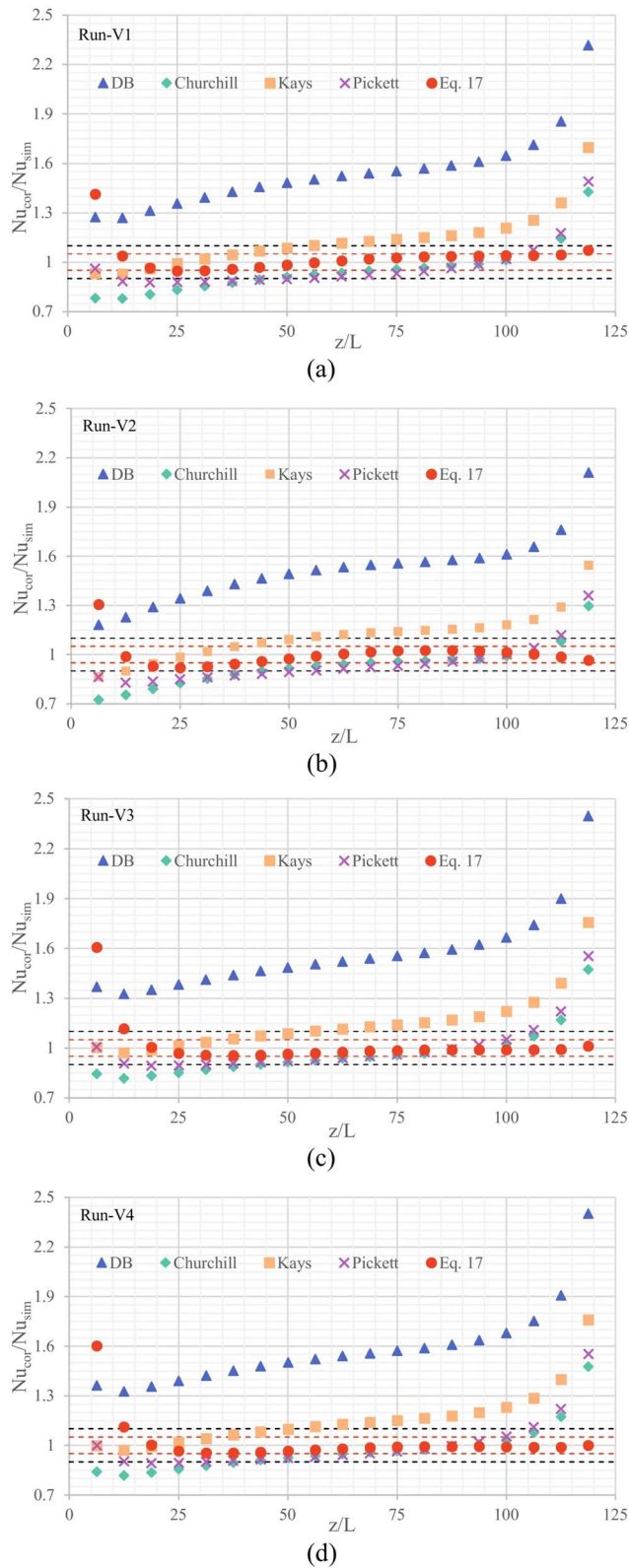


**Fig. 18** (Color online) Comparison of calculations using different equations based on simulation results of Run-V1 to Run-V4 (relative errors within red and black dashed lines are less than 5% and 10%, respectively). **a** Run-V1, **b** Run-V2, **c** Run-V3, **d** Run-V4

contrast to other correlations. The improved accuracy of Eq. 17, particularly near the outlet, can be attributed to the inclusion of the thermal boundary layer changes caused by power fluctuations, which were not considered in the other correlations. As the power decreases rapidly near the outlet, using a correlation that disregards changes in the thermal boundary layer may result in significant distortions in the calculations. Furthermore, consistent with the observed low accuracy of the calculations near the inlet, previous studies by Sparrow et al. [34] showed similar challenges in achieving accurate calculations in this region. They attributed the cause partially to changes in the fluid properties and the uncertainty of eddy diffusivities. However, in the present study, in addition to the reasons above, the simplification of formulas in the derivation process and the viscous dissipation caused by the high-speed fluid may result in inaccurate predictions near the inlet.

The preceding discussion highlights that although Eq. 17 provides satisfactory accuracy for most axial regions in the channel, further improvements can be realized. In this regard, the Kays correlation can be combined with Eq. 17 to derive a new segmented relationship, as shown in Eq. 21. To evaluate the effectiveness of the approach, Eq. 21 was applied to calculate the four operating conditions specified in Table 11, and the resulting calculation accuracy is presented in Fig. 19.

$$Nu = \begin{cases} 0.022Re^{0.8}Pr^{0.6} \left(\frac{z}{L} \leq 18.75\right) \\ 2\frac{\omega^2 + \pi^2}{\varphi\omega} \left\{ \pi \left[ \cot(\pi z) - \frac{1}{\sin(\pi z)\exp(\omega z)} \right] - \omega \right\}^{-1} \left(\frac{z}{L} > 18.75\right) \end{cases}$$

$$\varphi = -90.72Re_{avg}^{-0.72} \quad \omega = 1075.65Re_{avg}^{-0.31} \quad (21)$$

Equation 21 employs the Kays correlation to calculate  $Nu$  in the vicinity of the inlet ( $z/L \leq 18.75$ ). In this correlation,  $Re$  can be approximated using the principle of energy conservation. The  $Nu$  values in the remaining regions of the channel were calculated using Eq. 17. The data presented in Fig. 19 show a significant improvement in the prediction accuracy achieved via the optimized correlation (Eq. 21). Specifically, the maximum and average relative errors reduced to 13.3% and 2.9%, respectively, while a satisfactory level of accuracy was maintained throughout the channel axial range.

### 5 Conclusion

Numerical and theoretical investigations were conducted in this study to examine the heat transfer characteristics of a helium–xenon gas mixture in a cylindrical channel within a reactor core environment. A multiregion conjugated heat transfer model of the channel was established, and several

**Table 13** Relative error of calculation results using different correlations

		Dittus–Boelter	Churchill	Kays	Pickett	Equation 17
Relative error	Maximin (%)	140.2	47.7	76.1	55.4	60.6
	Average (%)	55.4	11.1	15.4	10.3	5.3

special operating conditions were designed to analyze the effects of these factors on  $Nu$ . The correlation for the axial  $Nu$  distribution in the channel was theoretically derived by assuming a cosine distribution for the axial power. Upon confirming the unknown coefficients, the accuracy of this correlation was meticulously examined and compared with those of other correlations. The main conclusions obtained were as follows:

1. The addition of a reflector at the inlet accelerated the axial decline rate of  $Nu$  near the inlet, whereas the addition of a reflector at the outlet presented the opposite effect, which enhanced  $Nu$  near the outlet. In the case of the cosine power distribution, the  $Nu$  near the inlet decreased significantly as the total power decreased, whereas the opposite trend was observed in the axial middle section of the channel.
2. Heat transfer was affected by the inlet temperature, inlet velocity, and outlet pressure through their effects on the overall  $Re$  of the channel. An increase in the inlet temperature resulted in a decrease in the overall axial  $Nu$ , whereas an increase in the inlet flow velocity or outlet pressure resulted in the opposite trend. Increasing the inlet velocity reduced the axial decline rate of  $Nu$  near the inlet, whereas simultaneously increasing both the power value and inlet velocity alleviated this phenomenon.
3. A theoretical correlation was established to calculate the axial distribution of  $Nu$  in a channel with cosine-distributed axial power. The coefficients used in the correla-

tion were determined based on simulation data, which resulted in a semi-empirical correlation.

4. Within the ranges of  $Re$  and  $Pr$  simulated in this study, the obtained semi-empirical correlation demonstrated a high degree of accuracy, with an average relative error of 5.3%. Moreover, by integrating the semi-empirical correlation with the Kays correlation, the overall relative error was further reduced to 2.9%, and the calculation accuracy was satisfactory across the entire axial range of the channel.

In future studies, a comprehensive approach encompassing both experiments and simulations shall be adopted to extensively investigate the heat transfer characteristics of the helium–xenon gas mixture. This approach contributes to the verification and expansion of the methodology outlined herein. Ultimately, the newly established correlation will serve as a foundation for the development of a subchannel analysis code designed specifically for helium–xenon cooled microreactors.

**Author contributions** All authors contributed to the study conception and design. Material preparation, data collection and analysis were performed by Tian-Shi Wang, Xiang Chai and Chao-Ran Guan. The first draft of the manuscript was written by Tian-Shi Wang and all authors commented on previous versions of the manuscript. All authors read and approved the final manuscript.

**Data availability** The data that support the findings of this study are openly available in Science Data Bank at <https://www.doi.org/10.57760/sciencedb.10957> and <https://cstr.cn/31253.11.sciencedb.10957>.

**Declarations**

**Conflict of interest** Xiao-Jing Liu is an editorial board member for Nuclear Science and Techniques and was not involved in the editorial review, or the decision to publish this article. All authors declare that there are no competing interests.

**References**

1. B. Zohuri, *Nuclear Micro Reactors* (Springer, Berlin, 2021)
2. Q. Yang, Q. Sun, X. Liu et al., Conceptual design and thermal-hydraulic analysis of a megawatt-level lead-bismuth cooling reactor for deep-sea exploration. *Prog. Nucl. Energ.* **145**, 104125 (2022). <https://doi.org/10.1016/j.pnucene.2022.104125>
3. L.S. Mason, A comparison of Brayton and stirling space nuclear power systems for power levels from 1 kilowatt to 10 megawatts. *AIP Conf. Proc.* (2001). <https://doi.org/10.1063/1.1358045>

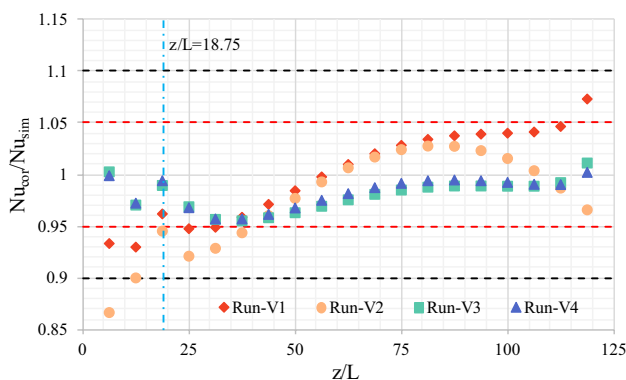


**Fig. 19** (Color online) Comparison of  $Nu$  between simulation data and Eq. 21 (relative errors within red and black dashed lines are less than 5% and 10%, respectively)

4. S.J. Bae, J. Lee, Y. Ahn et al., Preliminary studies of compact Brayton Cycle Performance for small modular high temperature gas-cooled reactor system. *Ann. Nucl. Energ.* **75**, 11–19 (2015). <https://doi.org/10.1016/j.anucene.2014.07.041>
5. R. Zhang, K. Guo, C. Wang et al., Thermal-hydraulic analysis of gas-cooled space nuclear reactor power system with closed Brayton cycle. *Int. J. Energ. Res.* **45**, 11851–11867 (2020). <https://doi.org/10.1002/er.5813>
6. C. Xu, F. Kong, D. Yu et al., Influence of non-ideal gas characteristics on working fluid properties and thermal cycle of space nuclear power generation system. *Energy* **222**, 119881 (2021). <https://doi.org/10.1016/j.energy.2021.119881>
7. B. Zhou, Y. Ji, J. Sun et al., Modified turbulent prandtl number model for helium–xenon gas mixture with low Prandtl number. *Nucl. Eng. Des.* **366**, 110738 (2020). <https://doi.org/10.1016/j.nucengdes.2020.110738>
8. J. Hilsenrath, Y.S. Touloukian, The viscosity, thermal conductivity, and Prandtl number for air, O<sub>2</sub>, N<sub>2</sub>, No, H<sub>2</sub>, CO, CO<sub>2</sub>, H<sub>2</sub>O, He, and A. *Int. Commun. Heat. Mass.* **76**, 967–983 (1954). <https://doi.org/10.1115/1.4015029>
9. X. Chai, X. Liu, J. Xiong et al., Numerical investigation of turbulent heat transfer properties at low prandtl number. *Front. Energy Res.* **8**, 112 (2020). <https://doi.org/10.3389/fenrg.2020.00112>
10. X. Cheng, N. Tak, Investigation on turbulent heat transfer to lead–bismuth eutectic flows in circular tubes for nuclear applications. *Nucl. Eng. Des.* **236**, 385–393 (2006). <https://doi.org/10.1016/j.nucengdes.2005.09.006>
11. M.F. Taylor, K.E. Bauer, D.M. McEligot, Internal forced convection to low-prandtl-number gas mixtures. *Int. J. Heat Mass Transf.* **31**, 13–25 (1988). [https://doi.org/10.1016/0017-9310\(88\)90218-9](https://doi.org/10.1016/0017-9310(88)90218-9)
12. V.E. Nakoryakov, S.L. Elistratov, O.V. Vitovsky et al., Experimental investigation of heat transfer in helium-xenon mixtures in triangle channels. *J. Eng. Thermophys.* **24**, 139–142 (2015). <https://doi.org/10.1134/s1810232815020046>
13. O.V. Vitovsky, S.L. Elistratov, M.S. Makarov et al., Heat transfer in a flow of gas mixture with low Prandtl number in triangular channels. *J. Eng. Thermophys.* **25**, 15–23 (2016). <https://doi.org/10.1134/s1810232816010021>
14. V.E. Nakoryakov, O.V. Vitovsky, Study of heat transfer of a helium–xenon mixture in heated channels with different cross-sectional shapes. *J. Appl. Mech. Tech. Phys.* **58**, 664–669 (2017). <https://doi.org/10.1134/s0021894417040101>
15. S.L. Elistratov, O.V. Vitovskii, E.Y. Slesareva, Experimental investigation of heat transfer of helium-xenon mixtures in cylindrical channels. *J. Eng. Thermophys.* **24**, 33–35 (2015). <https://doi.org/10.1134/s181023281501004x>
16. O.V. Vitovsky, V.E. Nakoryakov, E.Y. Slesareva, Heat transfer of helium–xenon mixture on the initial pipe section. *J. Eng. Thermophys.* **24**, 338–341 (2015). <https://doi.org/10.1134/s1810232815040062>
17. M.S. Makarov, O.V. Vitovsky, V.S. Naumkin et al., Investigation of hydraulic resistance and heat transfer in the flow of He-Xe mixture with a small Prandtl number in a quasi-triangular pipe. *Int. J. Heat Mass Transf.* **199**, 123427 (2022). <https://doi.org/10.1016/j.ijheatmasstransfer.2022.123427>
18. H. Qin, C. Wang, W. Tian et al., Experimental investigation on flow and heat transfer characteristics of He-Xe Gas Mixture. *Int. J. Heat Mass Transf.* **192**, 122942 (2022). <https://doi.org/10.1016/j.ijheatmasstransfer.2022.122942>
19. O.V. Vitovsky, M.S. Makarov, V.E. Nakoryakov et al., Heat transfer in a small diameter tube at high Reynolds Numbers. *Int. J. Heat Mass Transf.* **109**, 997–1003 (2017). <https://doi.org/10.1016/j.ijheatmasstransfer.2017.02.041>
20. V.G. Lushchik, M.S. Makarova, Heat transfer during the tube flow of an he–xe gas mixture with a substantial pressure gradient due to the strong heating of the tube. *J. Eng. Thermophys.* **95**, 1539–1547 (2022). <https://doi.org/10.1007/s10891-022-02622-8>
21. B. Zhou, Y. Ji, J. Sun et al., Nusselt number correlation for turbulent heat transfer of helium–xenon gas mixtures. *Nucl. Sci. Tech.* **32**, 128 (2021). <https://doi.org/10.1007/s41365-021-00972-1>
22. H. Qin, S. Qiu, C. Wang, Numerical investigation on heat transfer characteristics of helium-xenon gas mixture. *T. Am. Nucl. Soc.* (2019). <https://doi.org/10.13182/t31208>
23. D. Huang, Z. Li, L. Yu et al., Influence of helium-xenon mixing ratio on flow heat transfer characteristics of reactor channels. *J. Harbin Eng. Univ.* **42**, 745–750 (2021). <https://doi.org/10.11990/jheu.201909048>
24. S. Chen, H. Qin, C. Wang et al., Flow and heat transfer characteristic of He-Xe gas mixture with helical wire structure. *Atom. Energy Sci. Tech.* **55**, 990–999 (2021). <https://doi.org/10.7538/yzk.2020.youxian.0479> (in Chinese)
25. X. Shi, L. Wang, W. Chen et al., Effect of induced vortex and configuration layout on heat transfer enhancement of helium-xenon mixture. *Appl. Therm. Eng.* **225**, 120168 (2023). <https://doi.org/10.1016/j.applthermaleng.2023.120168>
26. T. Meng, K. Cheng, F. Zhao et al., Computational flow and heat transfer design and analysis for 1/12 gas-cooled space nuclear reactor. *Ann. Nucl. Energ.* **135**, 106986 (2020). <https://doi.org/10.1016/j.anucene.2019.106986>
27. Z. Duan, J. Zhang, Y. Wu et al., Multi-physics coupling analysis on neutronics, thermal hydraulic and mechanics characteristics of a nuclear thermal propulsion reactor. *Nucl. Eng. Des.* **399**, 112042 (2022). <https://doi.org/10.1016/j.nucengdes.2022.112042>
28. M. Yang, Q. Sun, C. Luo et al., Development and verification of a neutronics-thermal hydraulics coupling code with unstructured meshes neutron transport model. *Nucl. Tech.* **46**, 030601 (2023). <https://doi.org/10.11889/j.0253-3219.2023.hjs.46.030601> (in Chinese)
29. Z. Han, J. Zhang, M. Wang et al., A modified system analysis code for thermo-hydraulic calculation of hydrogen in a nuclear thermal propulsion (NTP) system. *Ann. Nucl. Energ.* **164**, 108632 (2021). <https://doi.org/10.1016/j.anucene.2021.108632>
30. Y.-B. Liu, X.-Y. Meng, X.-S. Wang et al., Transient analysis and optimization of passive residual heat removal heat exchanger in advanced nuclear power plant. *Nucl. Sci. Tech.* **33**, 106 (2022). <https://doi.org/10.1007/s41365-022-01083-1>
31. R. Lu, Z. Li, J. Zhao et al., Numerical investigation of heat transfer characteristics of high-speed and high-temperature air cooled open-cycle reactor. *Appl. Therm. Eng.* **179**, 115542 (2020). <https://doi.org/10.1016/j.applthermaleng.2020.115542>
32. Q. Sun, H. Zhang, Numerical study on heat transfer performance of cooling channels in space core. *Appl. Therm. Eng.* **210**, 118274 (2022). <https://doi.org/10.1016/j.applthermaleng.2022.118274>
33. A. Barletta, E. Zanchini, Laminar forced convection with sinusoidal wall heat flux distribution: axially periodic regime. *Heat Mass Transfer.* **31**, 41–48 (1995). <https://doi.org/10.1007/bf02537420>
34. E.M. Sparrow, T.M. Hallman, R. Siegel, Turbulent heat transfer in the thermal entrance region of a pipe with Uniform Heat Flux. *Appl. Sci. Res.* **7**, 37–52 (1957). <https://doi.org/10.1007/bf03184700>
35. R. Siegel, E.M. Sparrow, Turbulent flow in a circular tube with arbitrary internal heat sources and wall heat transfer. *J. Heat. Transf.* **81**, 280–287 (1959). <https://doi.org/10.1115/1.4008203>
36. A.P. Hatton, A. Quarmby, The effect of axially varying and unsymmetrical boundary conditions on heat transfer with turbulent flow between parallel plates. *Int. J. Heat Mass Transf.* **6**, 903–914 (1963). [https://doi.org/10.1016/0017-9310\(63\)90081-4](https://doi.org/10.1016/0017-9310(63)90081-4)
37. C.-J. Hsu, Heat transfer in a round tube with sinusoidal wall heat flux distribution. *AIChE J.* **11**, 690–695 (1965). <https://doi.org/10.1002/aic.690110423>

38. H. Shu, F. Yasunobu, Turbulent heat transfer in a tube with prescribed heat flux. *Int. J. Heat Mass Transf.* **11**, 943–962 (1968). [https://doi.org/10.1016/0017-9310\(68\)90001-x](https://doi.org/10.1016/0017-9310(68)90001-x)
39. C. Guan, X. Chai, T. Zhang et al., Preliminary lightweight core design analysis of a micro-transportable gas-cooled thermal reactor. *Int. J. Energ. Res.* **46**, 17416–17428 (2022). <https://doi.org/10.1002/er.8408>
40. M. Wang, Y. Wang, W. Tian et al., Recent progress of CFD applications in PWR Thermal Hydraulics Study and Future Directions. *Ann. Nucl. Energ.* **150**, 107836 (2021). <https://doi.org/10.1016/j.anucene.2020.107836>
41. W.-T. Li, X.-K. Meng, H.-Z. Bian et al., Numerical analysis of heat transfer enhancement on steam condensation in the presence of air outside the tube. *Nucl. Sci. Tech.* **33**, 100 (2022). <https://doi.org/10.1007/s41365-022-01090-2>
42. W.-H. Ji, J.-J. Cheng, H.-Z. Tao et al., Numerical simulation of coupling heat transfer and thermal stress for spent fuel dry storage cask with different power distribution and tilt angles. *Nucl. Sci. Tech.* **34**, 26 (2023). <https://doi.org/10.1007/s41365-023-01171-w>
43. W.M. Kays, Turbulent prandtl number—where are we? *J. Heat Transf.* **116**, 284–295 (1994). <https://doi.org/10.1115/1.2911398>
44. T. Barth, G. Lecrivain, S.T. Jayaraju et al., Particle deposition and resuspension in gas-cooled reactors—activity overview of the two European research projects THINS and ARCHER. *Nucl. Eng. Des.* **290**, 127–134 (2015). <https://doi.org/10.1016/j.nucengdes.2014.11.047>
45. C. Cheng, Z. Duan, W. Xu et al., Experimental study of the fouling deposition on heating surface of narrow rectangular channel. *Nucl. Tech.* **45**, 010601 (2022). <https://doi.org/10.11889/j.0253-3219.2022.hjs.45.010601> (in Chinese)
46. F.W. Dittus, L.M.K. Boelter, Heat transfer in automobile radiators of the tubular type. *Int. Commun. Heat Mass.* **12**, 3–22 (1985). [https://doi.org/10.1016/0735-1933\(85\)90003-x](https://doi.org/10.1016/0735-1933(85)90003-x)
47. S.W. Churchill, Comprehensive correlating equations for heat, mass and momentum transfer in fully developed flow in smooth tubes. *Ind. Eng. Chem. Fund.* **16**, 109–116 (1977). <https://doi.org/10.1021/i160061a021>
48. W.M. Kays, *Convective Heat and Mass Transfer* (McGraw-Hill, New York, 1980)
49. P.E. Pickett, M.F. Taylor, D.M. McEaligot, Heated turbulent flow of helium—argon mixtures in tubes. *Int. J. Heat Mass Transf.* **22**, 705–719 (1979). [https://doi.org/10.1016/0017-9310\(79\)90118-2](https://doi.org/10.1016/0017-9310(79)90118-2)

Springer Nature or its licensor (e.g. a society or other partner) holds exclusive rights to this article under a publishing agreement with the author(s) or other rightsholder(s); author self-archiving of the accepted manuscript version of this article is solely governed by the terms of such publishing agreement and applicable law.